Simulations of the response function of a plasma ion beam spectrometer for the Cassini mission to Saturn

J. H. Vilppola and P. J. Tanskanen
Department of Physics, University of Oulu, Oulu, FIN-90570, Finland

H. Huomo[a)]
Automation and Space Technology, VTT Technical Research Centre of Finland, P.O. Box 1303, FIN-02044 Espoo, Finland

B. L. Barraclough
Space and Atmospheric Sciences Group, Los Alamos National Laboratory, Los Alamos, New Mexico 87545

(Received 18 September 1995; accepted for publication 24 January 1996)

To obtain very high (~1%) energy resolution with spherical-section electrostatic analyzers requires high precision in both fabrication and in the alignment process. In order to aid in the calibration of the instrument and to help minimize fabrication costs, we have applied simulation models to the ion beam spectrometer for the NASA/ESA Cassini mission to Saturn. In our previous article we studied the effects of misalignment and simple irregularities of the hemispherical surfaces on the performance of an electrostatic analyzer. We have considered a hemispherical electrostatic analyzer equipped with an aperture plate to collimate the stray electric field at the entrance apertures. The influence of a curved entrance aperture has also been added to the simulation model, and its effects have been studied in detail. A cylindrical three-dimensional simultaneous overrelaxation algorithm has been introduced to solve for the stray electric field. The maximum loss of transmitted particles with respect to the transmission of an ideal instrument has been set at 10%. We demonstrate that the deviation in the distributions of the energies is less than 0.2% and that the deviation in the distributions of entrance angles of transmitted particles is less than 0.1°. It has been found that the energy resolution of an electrostatic analyzer can be improved from $\Delta E/E=(1.6\pm0.2)\%$ to $\Delta E/E=(1.3\pm0.2)\%$ by the introduction of front aperture plates. Through the introduction of curved entrance slits, the azimuthal angle resolution has changed from $\beta=(1.4\pm0.1)°$ for the simplified geometry simulation results of our previous article to $\beta=(2.3\pm0.1)°$. We have confirmed that an accuracy of 25 μm in the alignment of the two hemispherical surfaces is sufficient to give the instrument the desired resolutions. © *1996 American Institute of Physics.*
[S0034-6748(96)04604-2]

I. INTRODUCTION

The upcoming NASA/ESA observatory-class planetary mission for studying the Saturnian system is Cassini. The primary goal of the mission is to study Saturn, its moons and rings, and its magnetosphere. The mission has a planned launch date of late 1997, with an arrival at Saturn in 2004. The Cassini Plasma Science (CAPS) investigation[1] is currently being built to address numerous space physics science goals of the mission. CAPS consists of three carefully integrated sensors: the ion mass spectrometer (IMS), the electron spectrometer (ELS), and the ion beam spectrometer (IBS) which is the subject of this study.[2] The IBS is a high energy/angular resolution, a nearly 180° spherical section electrostatic analyzer that utilizes a unique crossed-fan viewing geometry to analyze ion beams expected during the course of the mission. The IBS uses three custom channel electron multipliers (CEMs) as detectors.[3]

In our previous article[4] (hereafter called paper I) the primary aim was to investigate the effects of manufacturing tolerances of the hemispherical analyzer plates. Thus, the stray electric field effects of the IBS were considered only as they affected ion energies. The geometrical properties of the hemispheres were estimated by calculating the trajectories of the ions after their entrance into the instrument. This article is a report of improvements in our simulation routines, which now take stray field effects into account, as well as the effects of the front aperture plate geometry and the shape of the apertures.

In paper I, it was shown that when a curved aperture is utilized (as opposed to an ideal straight aperture), the angles of the velocity vector of the incoming ions can become considerably intermixed. The azimuthal angle (β) is especially sensitive to mixing since it is limited to a smaller gap than the polar angle (α). The result of this mixing is known as a butterfly effect[5] as a plot of energy vs angle resembles a butterfly. Another source of perturbation is that of the stray electric fields near the entrance apertures. Naturally, when the stray field accelerates incoming ions it also changes the ion trajectories, and therefore the entrance angles of the incoming ions. A third identified source of perturbation is the geometry of the front aperture plate. With the front aperture plate installed in the IBS instrument, about 90% of the stray field can be confined to the volume between the front aperture plate and the hemispheres. Removal of the ions which collide with the front aperture plate, but otherwise could

[a)]Present address: Nokia Research Center, Radio Communications P.O. Box 45, FIN-00211 Helsinki, Finland.

 0034-6748/96/67(4)/1494/8/$10.00

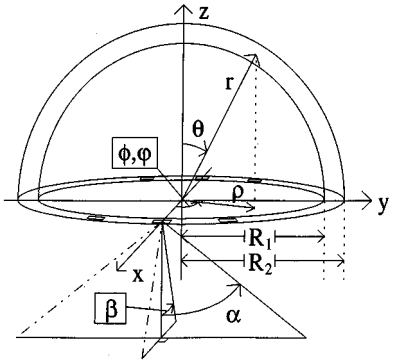

FIG. 1. Coordinate systems (x,y,z), (r,ϕ,θ), and (ρ,φ,z) angular variables α and β used for the initial velocity vector and parameters of the IBS instrument as appearing in the simulations. Inner radius R_1 is 0.098 75 m and outer radius R_2 is 0.101 25 m.

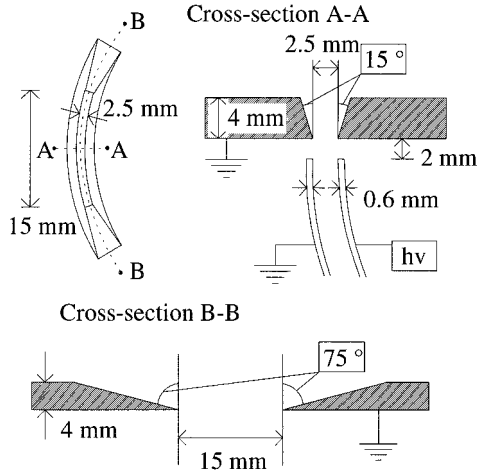

FIG. 2. Geometry of the IBS entrance aperture. On the left-hand side of the figure the aperture is seen from straight above the front aperture plate. Cross sections A–A and B–B are marked with dashed lines. Numeric values of the parameters of the geometry of the IBS entrance aperture are marked in the figure.

traverse the sensor, improves the energy resolution as well as the angular resolution of the instrument.

When all three identified sources of perturbation are included in our model, the energy resolution of the IBS changes from $\Delta E/E=(1.6\pm0.2)\%$, which was the result from our previous simulation, to $\Delta E/E=(1.3\pm0.2)\%$. Correspondingly, the azimuthal angular resolution changes from $\beta=(1.4\pm0.1)°$ to $\beta=(2.3\pm0.1)°$, mainly because of the butterfly effect. There is no substantial change in the one-dimensional 1D polar angle (α) distribution. In Sec. II, we give the theory and algorithms used for the new simulation routines. Section III presents the results and finally in Sec. IV we discuss the results and the future of our simulation routines, as well as possible modifications that might be made during fabrication of the IBS instrument.

II. THEORY AND ALGORITHMS FOR SIMULATIONS

In this article we use some of the basic concepts developed in paper I. All three IBS apertures shown in Fig. 1 are identical. Thus for convenience, we can consider the instrument a single aperture, spherical section electrostatic analyzer. The results can be generalized for the actual IBS instrument by a 30° coordinate rotation in the xy plane. All three coordinate systems, shown in Fig. 1, are chosen so that the xy-plane at $z=0$ lies at the edges of the hemispheres, the z axis points towards the top of the hemispheres, and the x axis passes through the center of the aperture.

Figure 2 shows the cross section of one of the apertures. The front aperture plate controls the angular range of incoming ions that are accepted. The simulation method developed in paper I is also applied here. In each Runge–Kutta step, the position of a particle transiting the analyzer is defined and its position with respect to the front aperture plate can be verified. Between each Runge–Kutta step the ion trajectories are approximated as straight lines and possible ion collisions with the front aperture plate are checked. If such a collision occurs, the particle is lost.

In the stray field area, the ion trajectories have to be solved numerically. The method used in the new simulations is based on the Laplace equation[6] $\nabla^2 V=0$, applied to the space between the hemispherical electrodes and the front aperture plate, as well as the space just outside of it. Thus, the electric potential is defined by the negative high voltage on the inner hemisphere, the grounded outer hemisphere, and the front aperture plate (see Fig. 2). The vacuum at infinity is also at ground potential. In practice, the potential can be adequately calculated, if we assume ground potential at a finite distance instead of infinity. It is presumed that this distance is far enough from the front aperture plate so that the zero potential can be used safely. To calculate the potential, the continous space is replaced by a finite potential mesh. The Laplace equation yields an approximate value for the potential. If the boundary value[7] method is used to calculate the potential outside the front aperture plate, the boundary of the far ground potential has to be set in advance, and its distance determined so as to satisfy the accuracy requirements. This is accomplished through iteration.

The boundary conditions for the iteration process are set using the geometry shown in Fig. 2. The mesh points inside the front aperture plate and the outer hemisphere are set to ground potential, and the mesh points inside the inner hemisphere are set to the negative high voltage. The mesh points between the hemispheres are handled as boundary points, and the initial potential at those points are calculated using the spherical equation[6]

$$V(\rho,\varphi,z=0)=V(r)=hv\left(\frac{1}{r}-\frac{1}{R_2}\right)/\left(\frac{1}{R_1}-\frac{1}{R_2}\right), \qquad (1)$$

where hv is the negative high voltage on the inner hemispheres and the other symbols are defined in Figs. 1 and 2. The potential mesh is set so that the hemispherical side border is at some positive z value so that the boundary points which are outside the hemispheres do not affect the points just above the hemispheres. Only the points in the space between the hemispheres and the front aperture plate are checked, since the acceptable ion trajectories are limited to that area. Here the value $z=0$ is still a good value for the mesh boundary, with analytical values given by Eq. (1).

The simultaneous overrelaxation (SOR)[7] method is used to solve for the potential numerically. The two-dimensional version of the routine, as given by Press *et al.*,[7] is expanded into a three-dimensional algorithm in cylindrical coordinates (ρ,φ,z) (see Fig. 1). To save computer time, the Chebyshev acceleration with odd–even ordering for the mesh points is used.[7] The iteration for each mesh point has to be continued until the desired accuracy is achieved. Finally, the mesh is fully relaxed and the values of the potential at each mesh point are as close to the correct potential as it is possible to come using the algorithm.

The potential is known with reasonable accuracy only at the mesh points. If the mesh points are sufficiently close together it can be assumed that the potential is linear inside the primitive cube, and the potential values can be calculated as the weighted average of the eight nearest mesh points. As a result of aperture symmetry the number of mesh points is reduced to one-half. The applied symmetry yields for the potential $V(\rho,\varphi,z)=V(\rho,-\varphi,z)$. Thus, only the potential for the positive side of the mesh has to be calculated. If the potential is symmetric in the φ direction, the partial derivative $\partial V/\partial\varphi$ is antisymmetric. The partial derivatives can be used when numerically solving the three-dimensional equation of motion in cylindrical coordinates.[8,9] This gives the equation of motion

$$\ddot{\rho}=\rho\dot{\varphi}^2-\frac{q}{m}\frac{\partial V}{\partial\rho}, \tag{2a}$$

$$\ddot{\varphi}=-\frac{2\dot{\rho}\dot{\varphi}}{\rho}-\frac{q}{m\rho^2}\frac{\partial V}{\partial\varphi}, \tag{2b}$$

and

$$\ddot{z}=-\frac{q}{m}\frac{\partial V}{\partial z}, \tag{2c}$$

where m is the mass and q is the charge of the ion. The fourth order Runge–Kutta algorithm[7] can be used to solve Eqs. (2a)–(2c). The initial values for a hemispherical routine, introduced in paper I, is calculated using the output values of the stray field routine given above.

Because of the ''mixing of the entrance angles'' of the velocity vector of the incoming ions, the effect of the curved aperture has to be considered when the ions pass from the stray field area into the hemispherical area of the instrument. This is done by eliminating those ions from the calculations which collide with the front aperture plate. In paper I we considered the aperture as a very thin straight slit along the x axis (see Fig. 1). Thus, all ions had the same initial value $\varphi=0$. Since the stray field routine gives a range of values for φ, a transformation of angles α and β (see Fig. 1) has to be made for a direct application of the two-dimensional routine. The required transformation is

$$\alpha'=\arcsin(\sin\beta\,\sin\varphi+\sin\alpha\,\cos\varphi), \tag{3a}$$

$$\beta'=\arcsin(\sin\beta\,\cos\varphi-\sin\alpha\,\sin\varphi), \tag{3b}$$

where α' and β' are the angles of the initial velocity vector perpendicular (α') and parallel (β') to the 2D plate where the ion trajectory is inside the spherical field of the hemispherical condenser.[5,10] Since the length of the aperture limits the angle φ, it can be used when defining the ion optics of the instrument. As a compromise one obtains a longer aperture with more throughput and angle mixing, and a shorter aperture with fewer accepted particles but less angular mixing.

The ion trajectories can now be calculated using a Monte Carlo simulation to determine the real transmission characteristics of the IBS instrument. In paper I, random values for initial ion parameters were given and a flat spectrum was used for all these parameters. In the present simulations the properties of the laboratory ion beam used for instrument calibration have been defined by the distance between the ion source and the entrance slit, the width of the ion beam, the energy resolution and angular collimation of the ion beam, as well as the sighting point of the ion beam in IBS coordinates. The angular and energy distributions of the laboratory ion beam have to be known if the beam is to be properly simulated. In our case a white spectrum is used for the beam distributions. For each set of ion beam variables (α,β,E) a given number of ions is injected and the number of ions transmitted through the analyzer is inserted into the appropriate location in the 3D matrix approximately describing the IBS response function. The indices of the matrix are directly proportional to the laboratory ion beam variables (α,β,E). With this ion beam simulation a simulation of the actual laboratory calibration conditions can be made.

The potential between the plates is directly proportional to the energy/charge ratio of the ions transmitted. In our simulations we have fixed the energy $E=E_{0h}$ of the proton (or the ion with same energy/charge ratio) which has a circular orbit with radius $r=R_{\mathrm{mid}}$ in the space between the hemispheres. E_{0h} defines the high voltage, hv, of the inner hemisphere with respect to the outer, which is grounded. The potential hv between the electrodes can be written

$$hv=-\frac{2E_{0h}R_{\mathrm{mid}}(R_2-R_1)}{qR_1R_2}, \tag{4}$$

where q is the ion charge, and R_1 and R_2 are defined in Fig. 1. The stray field accelerates the ions, and the average ion energy E_0 can be calculated from the equation

$$E_0=E_{0h}\left(\frac{2R_{\mathrm{mid}}}{R_2}-1\right). \tag{5}$$

E_0 is equivalent to the nominal kinetic energy in paper I. All energies are expressed as relative deviations from E_0. The energy resolution can be studied either by fixing the high voltage and letting the ion beam energy vary, or by varying the high voltage for a fixed energy ion beam as is actually done in laboratory calibrations.

III. RESULTS OF SIMULATIONS

In the present article, we have studied the ideal case corresponding to an instrument with perfect geometry, and cases where linear misalignments in each main coordinate axis x, y, and z occurred (see Fig. 1). The effects of indentations of the hemispheres were not considered, since the results presented in paper I are still valid. The misalignments are defined so that the coordinate systems shown in Fig. 1

TABLE I. The values of the parameters used in the simulation of the laboratory ion beam.

Distance between ion source and IBS aperture	2.10 m
Width of ion beam (at ion source)	16.0 mm
Energy spread of ion beam	±0.1%
Divergence of ion beam	±0.1°
x coordinate of sighting point	0.1000 m
y coordinate of sighting point	0.0000 m
z coordinate of sighting point	−0.0060 m
Nominal kinetic energy (E_{0h}! Please see definition in Sec. II)	100 eV
Maximum and minium α angle for ion beam	±75°
Step size of ion beam in α direction	3.0°
Maximum and minimum β angle for ion beam	±3.0°
Step size of ion beam in β direction	0.12°
Maximum and minimum middle energy (of nominal) for ion beam	±3.0%
Step size of middle energy	0.12%

are fixed to the outer hemisphere, and the inner hemisphere is shifted. The relative shifts in any direction can be studied using the misalignments with respect to the main coordinate axes x, y, and z.

The values of the parameters for the laboratory ion beam are presented in Table I, where the width of the ion beam is such that it covers the whole aperture for every possible setting of angles α and β. This corresponds to the actual laboratory situation. The requirements of the stray field calculations given in Sec. II are fulfilled using the potential mesh parameters shown in Table II. Also given is the value for the spectral radius of the Jacobi iteration ρ_{Jacobi}, which is used in the Chebyshev acceleration[7] to calculate the overrelaxation parameter. The maximum error of the mesh point after relaxation determines the accuracy used in the relaxation calculations. The symbols of the IBS instrument parameters as well as their values used in the simulations are presented in Figs. 1 and 2. The cross section of the calculated 3D potential mesh at the plate $\phi=0°$ is shown in Fig. 3. The figure shows a smooth behavior of the field lines particularly in the area above the entrance slit. This assures us that the results of our simulations for particles in the stray field area are reliable. In the actual IBS, the center of the hemispheres is 2 mm above the plate tangential to the edges of the hemispheres. Thus, the real reverse angle of the IBS flight model is only about 178° instead of 180° which is the definition of hemispherical analyzer. This means that the β angles used in our simulations can be used for the actual IBS only after a correction of 2 mm/100 mm rad has been subtracted.

TABLE II. The parameters of the potential mesh and the parameters of the overrelaxation calculation as used in the simulations.

Size of mesh (points)	100×100×100
Minimum value of coordinate ρ (=mesh edge)	0.097 50 m
Maximum value of coordinate ρ	0.102 50 m
Minimum value of coordinate φ (note symmetry!)	0.00 rad
Maximum value of coordinate φ	0.50 rad
Minimum value of coordinate z	−0.017 m
Maximum value of coordinate z	0.001 m
Spectral radius of the Jacobi iteration ρ_{Jacobi} (see Ref. 7)	0.985
Maximum relative error of mesh points after relaxation	1×10^{-10}

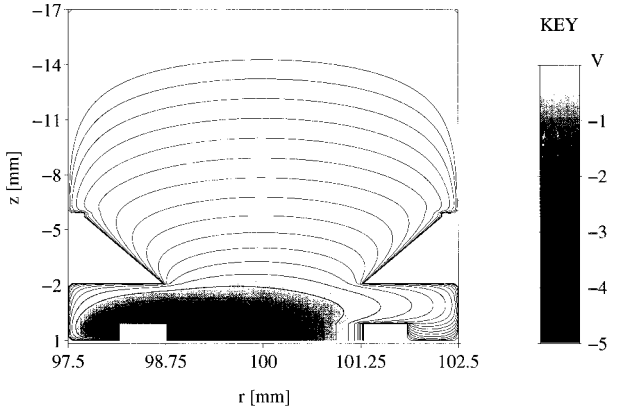

FIG. 3. Cross section of the 3D potential mesh of the IBS stray field potential with constant value for $\varphi=0.0°$ (see also Figs. 1 and 2). Key shows the gray scale potential distribution in volts. Potential drops by a factor of 2 between adjacent contours (or between the $h\nu$ electrode and the first contour).

The simulations were made for the ideal case, and for cases of 25 and 60 μm misalignments along the direction of the main coordinate axes. In every simulation at each ion beam setting (α,β,E) 250 ions were injected. Since there are 51 different values for each of these variables, a total of 33 162 750 (=51×51×51×250) ions per simulation are injected. An exception had to be made when the cut through at IBS response function was studied for the parameters α, β, and E. To avoid excess random noise the beam intensity was increased by a factor of 10. The simulation was made once for each parameter, yielding a total number of 19 507 500 (=3×51×51×2500) injected ions per each studied case of misalignment.

The transmission percentages, similar to the ones presented in paper I, could not be calculated from the simulation results, because of the differences in the random ion injection algorithms. Instead, the relative transmissions with respect to an ideal case were calculated in each simulated case, and the results shown in Table III. Shown also are the average energy and the average value of β of the distributions together with their full width at the half-maximum (FWHM) values.

The energy distributions as well as the distributions of the initial angles α and β in the ideal case and the case of 60 μm misalignment are shown in Fig. 4. The distributions have been calculated by summing up the indices from the three-

TABLE III. The full width at half-maximum (FWHM) values, the average energy E and angle β distributions and transmission percentages in the ideal case, and in the case of 25 and 60 μm misalignment in x, y, or z directions. The transmissions are given with respect to the transmission in the ideal case.

Error	FWHM_E (%)	Ave_E (%)	FWHM_β (deg)	Ave_β (deg)	Transm.
ideal	1.3	0.12	2.3	0.24	1.000
25 μm x shift	1.3	0.12	2.3	0.60	0.920
60 μm x shift	1.1	0.12	2.0	1.20	0.590
25 μm y shift	1.7	0.06	2.2	0.18	0.999
60 μm y shift	3.5	0.12	2.2	0.18	0.989
25 μm z shift	1.3	0.84	2.2	0.06	0.989
60 μm z shift	1.4	1.86	2.2	−0.18	0.953

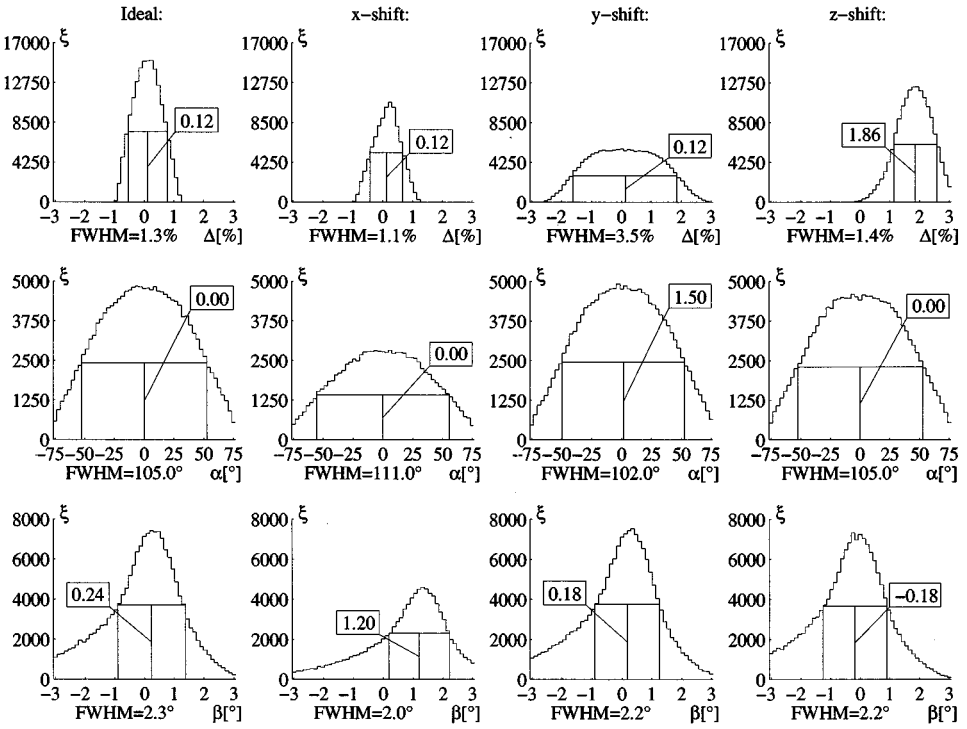

FIG. 4. Energy distributions and the distributions of the angles α and β in an ideal case and in cases when a 60 μm misalignment in either the x, y, or z direction has occurred. Full width at half-maximum (FWHM) values and the average of the distributions are shown for all distributions. $\Delta=(E-E_0)/E_0$ where E_0 is the nominal kinetic energy. ξ=number of transmitted particles per bin. Bin widths are $\delta E=0.12\%$, $\delta\alpha=3.0°$, and $\delta\beta=0.12°$.

dimensional data matrix and the results have been presented as one-dimensional distributions. This method of handling ''the invisible parameters'' is called ''the white spectrum method.'' The energy and the angle β distributions are comparable to the ones presented in paper I. The α distributions can also be directly compared after the values shown in Fig. 4 have been divided by cos α. The FWHM for the α distribution shown in Fig. 4 can be used when considering the different shapes of the α distributions.

Figures 5 through 8 show two-dimensional distributions using different parameter pairs and two different methods of analyses for an ideal case and in the case of 25 μm misalignments when these have caused appreciable changes in the distributions. The E/β distributions using a white spectrum for the invisible parameter α are shown in Fig. 5. The E/β distribution for an ideal case using a cut through for the parameter α is shown in Fig. 6. The values of all cut through parameters are proportional to the indices which give maximum transmission using statistical averaging instead of using the real maximum. Otherwise the random noise might effect the cut selection as can be seen in profile plot selections where the actual maximum has been used. For example, in Fig. 5 in the $dx=25$ μm plot, the β profile is not exactly at the middle of the two-dimensional distribution. The definition of the cut through for an invisible parameter using statistical averaging is later called a cut through method. The cut through E/α distributions are shown in Fig. 7, and the cut through α/β distribution for an ideal case is shown in Fig. 8. The white spectrum E/α and α/β distributions as well as the 25 μm misalignment cut through distributions resemble those shown in Figs. 7 and 8.

The butterfly effect has been considered as a separate problem. The maximum and minimum transmission angles of the initial velocity vector are studied as a function of the length of the aperture. The results for the angle β are pre-

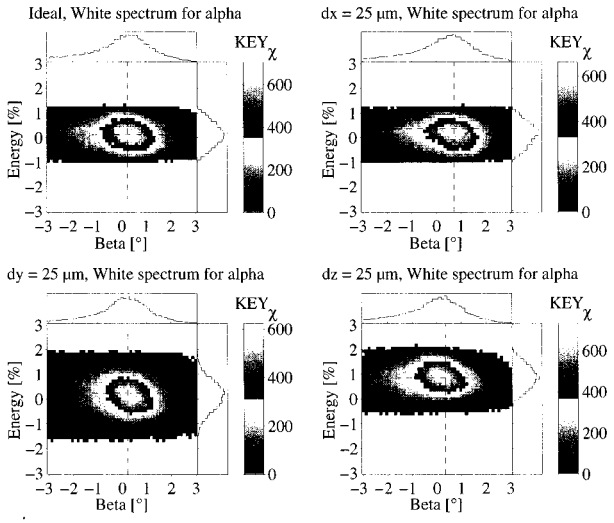

FIG. 5. Energy/beta (E/β in the text) distributions using a white spectrum for the invisible parameter α in an ideal case and in cases when a 25 μm misalignment in either the x, y, or z direction has occurred. ξ=number of particles transmitted per bin square. Key shows the gray scales to the ξ numbers. Bin widths are identical to ones in Fig. 4. Energy is the same as the symbol Δ in Fig. 4. Dashed cross shows the bin square where the transmission has it maximum. Dashed lines shows the bins, which have been used to produce the profile plots at the upper and right-hand sides of each single gray scale plot. Gray scales in each plot have been chosen so that the inner black ring shows the bin squares with full width at half-maximum values.

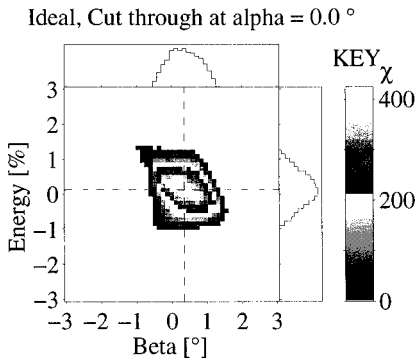

FIG. 6. Energy/beta (E/β in the text) distribution using cut through for the invisible parameter α in an ideal case. Cut through value proportional to the cut through index is shown in the figure. Possible changes of particle distributions due to misalignments are given in the text. Other symbols are similar to the ones in Figs. 4 and 5.

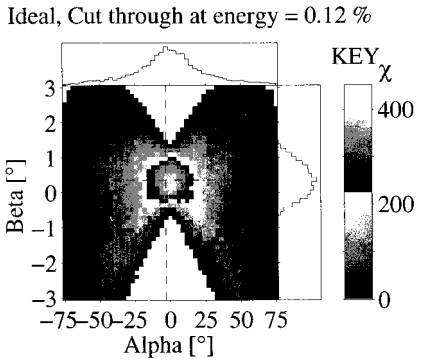

FIG. 8. Alpha/beta (α/β in the text) distribution using cut through for the invisible parameter energy in an ideal case. Possible changes of particle distributions due to misalignments are given in the text. Other symbols are similar to the ones in Figs. 4, 5, and 6.

sented in Fig. 9. The angle β has been solved from Eqs. (11a) and (11b) as a function of angles α', β', and φ. The maximum and the minimum value for the angle β can be calculated for different maximum and minimum values of α', β', and φ. The maximum and minimum values of β' are defined by using the β values for $\alpha=0°$ (Fig. 8) where no butterfly effect is present. The values used in our calculations are then $\beta'_{\min} = -0.82°$ and $\beta'_{\max} = 1.56°$, $\alpha'_{\min} = -75°$ and $\alpha'_{\max} = 75°$. The maximum [or minimum] angle φ is defined using the radius corresponding to the center of the space between hemispheres (=0.100 mm) and the length of the aperture as $\varphi_{[\min],\max}=[-](\text{length}/2)/(\text{radius})$.

IV. DISCUSSION

The cross section of the 3D stray field potential mesh at the plate $\phi=0°$ presented in Fig. 3 shows the shape of the approximate potential function. With the chosen parameter values of the mesh, the potential behaves smoothly within the volume where these ions move that do not collide with the front aperture plate. When considering the contours, which are spaced so that the potential drops by one-half between adjacent contour lines, it can be noticed that about 90% of the stray field is collimated into the volume between the front aperture plate and the hemispheres. Above the front aperture plate the potential rapidly approaches zero. The accuracy of the potential net can be influenced by changing the values of the parameters shown in Table II. The higher the point density the higher the accuracy, and the larger the net, the more realistic is the estimated potential outside the IBS. The values in Table II give good estimates for the potential, especially in the most important stray field area which is the volume between the front aperture plate and the hemispheres (the darkest area in the Fig. 3).

The maximum misalignment of 25 μm for the hemispheres given in paper I is still valid, since the relative changes from an ideal case to each of the misalignment cases are quite similar. This can be seen when comparing Table III and Fig. 4 in this article with Table II and Fig. 5 in paper I. We feel we now have a much better estimate of the energy resolution than in paper I. This is because we have incorporated the front aperture plate which cuts off ions with relative energies that are too high or too low. On the other hand, in the β distribution (Fig. 8), the changes in the FWHM values imply a loss of angular resolution in the one-dimensional

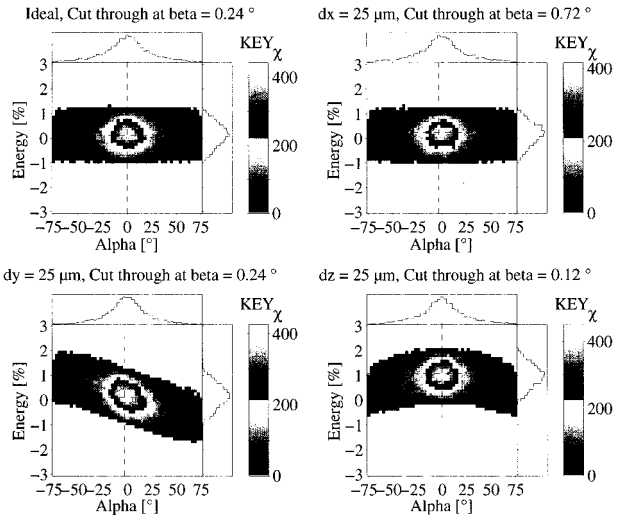

FIG. 7. Energy/alpha (E/α in the text) distributions using cut through for the invisible parameter β in an ideal case and in cases when a 25 μm misalignment in either the x, y, or z direction has occurred. Other symbols are similar to the ones in Figs. 4, 5, and 6.

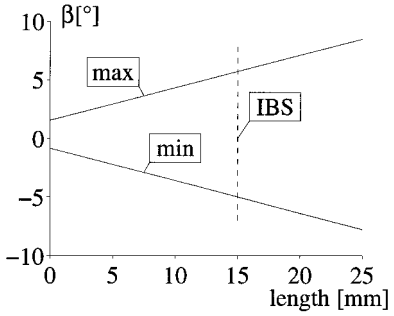

FIG. 9. Maximum and minimum initial β angle as a function of the length of the aperture for ions traveling through a hemispherical electrostatic analyzer calculated by using Eqs. (11a) and (11b) in the ideal case. Aperture length of the IBS instrument is marked with a dashed line. This effect is due to the finite aperture curvature (butterfly effect).

distribution. This is a result of the curved aperture and the accompanying butterfly effect. In the α distributions, a clear cosine dependence is obvious. The cosine form of the distributions was introduced through the stray field routine. Ions with larger α and β angles are more likely to collide with the front aperture plate than ions with smaller angles. This creates the cosinelike α distributions. The stray field, and especially the misalignments twist the shape of the α distributions as can be seen when comparing the different FWHM values for each α distribution in Fig. 4. The perturbations can be estimated to be as wide as the bin widths. The differences in distributions obtained in paper I and the new simulations considered above still remain, since the differences are systematically the same in magnitude in all the distributions.

The errors due to manufacturing/assembly found in this study are similar to those found in paper I. The spread in the relative energy distribution shown in Fig. 5 is very obvious for the misalignment in the y direction ($dy=25$ μm). Since we cannot *a priori* predict the actual misalignment, the exact energy resolution of the IBS instrument has to be determined through calibrations. This parameter is required for the development of the flight software. From the calculations of the cut through E/β distributions, shown in Fig. 6 for an ideal case, it could be deduced that the shape of the distributions remained constant for 25 μm shifts along all three axes. This is to be expected, since a misalignment in the y direction has no effect for a fixed value of α. Figure 5 shows that the width of the energy distribution is similar to the result obtained for the one-dimensional distribution in paper I. This also clearly shows that the white spectrum method has to be considered in the calibrations to obtain the best possible results.

Notable twists can be seen in the $dy=25$ μm and the $dz=25$ μm cut through E/α plots in Fig. 7, while the $dx=25$ μm plot is almost identical to the ideal plot. In the $dy=25$ μm plot, a small rotation is present, and in the $dz=25$ μm plot the distribution has a curved shape. In both cases this is to be expected since, if the hemispheres are displaced in these directions, the transition is perpendicular with respect to the ion trajectories, and thus the distances between the hemispheres have different values for different α angles. In the case of the misalignment in the y direction the ions with positive α angles enter an area where the hemispheres are further apart and thus experience a weaker force than ions with negative α angles. This effect decreases the transmission energy for the positive α angles and increases it for the negative ones. This applies for the misalignment in the z direction as well. The effect reaches a maximum value for $\alpha=0°$. The magnitude of this effect can be seen in the $dy=25$ μm and the $dz=25$ μm plots in Fig. 7. When comparing the errors in Figs. 5 and 7, the same effect can be seen. Figure 7 shows that the energy resolution remains unchanged, but the center energy varies as a function of the α angle. This gives some hope that an offset problem might be corrected with the help of the calibration and by modifications to the flight software, while the energy resolution of the IBS still remains the same as in the ideal case. When considering the corresponding white spectrum E/α distributions, similar conclusions can reached.

The effects due to the curved aperture can be studied using the α/β distribution shown in Fig. 8 for an ideal case. The distributions when 25 μm shifts in x, y, and z directions were allowed show an almost identical spread in the β direction similar to the one shown for the ideal case. The only change is seen in the $dx=25$ μm plot, where the FWHM ring has moved to higher values of angle β. This can easily be taken care of in the calibration process. The corresponding white spectrum figure yields the same results. The situation remains the same when considering the corresponding cases for the 60 μm misalignments. Since the energies are now twisted even more than in the 25 μm misalignment case shown in Fig. 7, the cut through a specific energy value excludes ions transmitted with large α angles. For the misalignment in the z direction this means a loss of particles in a couple of bin squares in both the negative and positive edges of the α direction. For the misalignment in the y direction particle losses occur in bin squares, where $\alpha<-25°$ and $\alpha>40°$. We can again safely predict that in the case of the α/β figures the error will be linear when considering the different kind of misalignments. Since the butterfly effect is now present in all cases, it has to be considered in the calibrations and in the development of the flight software. We have included Fig. 9 to show the butterfly effect together with the effect of an increased aperture length. Since no stray field effects or different front aperture plate geometries have been considered in Fig. 9, the numbers may not be exact but they can be used for different aperture lengths by using the 15 mm aperture length as a reference point. As can be seen in Fig. 9, the width of the β distributions increases linearly as a function of the aperture length. The FWHM rings are quite small with respect to the ''wing sizes'' of the butterfly as can be seen in Fig. 8. Therefore it can be stated that a long aperture introduces noise for large values of α. On the other hand for a given ion flux, more ions will be transmitted for small values of α. Thus the final aperture length has to be chosen as a compromise between a longer aperture with more throughput and more ''noise,'' and a shorter aperture with fewer transmitted ions and less noise. In the case of the IBS instrument to be used in the Saturnian environment with low ion fluxes, a long aperture length yielding a clear butterfly effect has to be accepted.

ACKNOWLEDGMENTS

The authors would like to acknowledge University of Oulu, the Academy of Finland, the Ministry of Trade and Industry of Finland, VTT Technical Research Centre, and NASA for financial support of the project. The authors would like to thank Dr. J. T. Gosling and Dr. D. J. McComas for their valuable comments and suggestions.

[1] NASA, A Proposal for the Plasma Science (PLS) Investigation for the Cassini Orbiter Spacecraft, Volume 1: Investigation and Technical Plan, SwRI Proposal 15-9376.
[2] S. J. Bame, D. J. McComas, D. T. Young, and R. D. Belian, Rev. Sci. Instrum. **57**, 1711 (1986).
[3] D. J. McComas, J. R. Baldonado, S. J. Bame, and B. L. Barraclough, Rev. Sci. Instrum. **58**, 2331 (1987).
[4] J. H. Vilppola, J. T. Keisala, P. J. Tanskanen, and H. Huomo, Rev. Sci. Instrum. **64**, 2190 (1993).

[5] J. T. Gosling, M. F. Thomsen, and R. C. Anderson, Los Alamos National Laboratory Report LA-12962-MS, 1984.
[6] I. S. Grant and W. R. Phillips, *Electromagnetism* (Wiley, New York, 1976).
[7] W. H. Press, B. P. Flannery, S. A. Teukolsky, and W. T. Vetterling, *Numerical Recipes, The Art of Scientific Computing* (Cambridge University Press, Cambridge, 1986).
[8] M. R. Spiegel, *Theory and Problems of Vector Analysis and an Introduction to Tensor Analysis* (McGraw–Hill, New York, 1959).
[9] G. Arfken, *Mathematical Methods for Physicists* (Academic, San Diego, 1985).
[10] J. T. Gosling, J. R. Asbridge, S. J. Bame, and W. C. Feldman, Rev. Sci. Instrum. **49**, 1260 (1978).